

To be published in Applied Optics:

Title: Characterizing turbulence profile layers through celestial single-source observations

Authors: Douglas Laidlaw, Andrew Reeves, Ramon Mata Calvo, Himanshi Singhal

Accepted: 06 December 21

Posted 10 December 21

DOI: <https://doi.org/10.1364/AO.443698>

© 2021 Optica

OPTICA
PUBLISHING GROUP
Formerly OSA

Characterizing turbulence profile layers through celestial single-source observations

DOUGLAS J. LAIDLAW,^{1,*} ANDREW P. REEVES,¹ HIMANSHI SINGHAL,^{1,2} AND RAMON MATA CALVO¹

¹ Institute of Communications and Navigation, German Aerospace Center (DLR), 82234, Weßling, Germany

² Department of Aerospace and Geodesy, Technical University of Munich (TUM), 80333, Munich, Germany

* douglas.laidlaw@dlr.de

Abstract: Future spacecraft missions aim to communicate with the Earth using near-infrared lasers. The possible bit rate of Free-Space Optical Communication (FSOC) is orders of magnitude greater when compared to current Radio Frequency (RF) transmissions. The challenge of ground-space FSOC is that atmospheric turbulence perturbs optical wavefront propagation. These wavefront aberrations can be measured using a Shack-Hartmann Wavefront Sensor (SHWFS). A ground-based Adaptive Optics (AO) system can mitigate these aberrations along the optical path by translating wavefront measurements into Deformable Mirror (DM) commands. However, errors result from atmospheric turbulence continuously evolving and there being unavoidable delays during AO wavefront correction. The length of an acceptable delay is referred to as the coherence time - a parameter dependent on the strength of turbulence profile layers and their corresponding wind-driven velocity. This study introduces a novel technique for using SHWFS single-source observations, e.g. the downlink signal from a geostationary satellite, to measure the strength and velocity of turbulence profile layers. This work builds upon previous research and demonstrates that single-source observations can disentangle turbulence profile layers through studying the cross-covariance of temporally offset SHWFS centroid measurements. Simulated data is used to verify that the technique can recover the coherence time. The expected and measured results have a correlation coefficient of 0.95.

© 2021 Optical Society of America under the terms of the [OSA Open Access Publishing Agreement](#)

1. Introduction

It is conventional for spacecraft and Earth-based stations to communicate using Radio Frequency (RF) transmissions. At these wavelengths the atmosphere is transparent. However, RF transmissions have a relatively large beam divergence and therefore the communicated signal can be easily intercepted. Free-Space Optical Communication (FSOC) offers an alternative to RF. This technology uses near-infrared lasers and is inherently more secure because its channels have a lower beam divergence. The possible bit rate of FSOC is also orders of magnitude greater than an RF channel. This enables future space missions to efficiently receive and transmit much larger data packets. A network of Optical Ground Stations (OGSs) would therefore facilitate this technology to outcome cloud cover limitations and provide worldwide high-speed internet. A further advantage of ground-space FSOC is that the required terminals are more compact and consume less energy than conventional RF systems. This makes FSOC a cost-effective option for future technologies.

At the top of the atmosphere the optical wavefront from a celestial object is considered flat. As this optical signal then propagates through the atmosphere it becomes distorted and suffers from severe amplitude fluctuations. This degradation is caused by the channel having an unstable refractive index due to the constant mixing of different air temperatures. There are two observable effects when monitoring the celestial object from the ground: its wavefront has deformations (first order) and local focussing errors (second order). The first order effect limits the angular resolution of ground-based telescopes and causes sections of the wavefront to have different

tip-tilt phase aberrations. The second order effect results in spatial intensity fluctuations across the pupil plane of a telescope and is referred to as scintillation. Both of these effects can critically destabilize FSOC channels, thereby preventing ground-space links from being established.

A proposed solution for mitigating the effects of atmospheric turbulence is for OGSs to employ Adaptive Optics (AO) technology. It is common for an AO systems to include a Shack-Hartmann Wavefront Sensor (SHWFS). This instrument is used to monitor the light from a celestial object and measure wavefront aberrations caused by atmospheric turbulence. The AO system can then use these measurements to run a Deformable Mirror (DM) such that it performs real-time wavefront reconstruction. A technique for operating the DM requires the interaction matrix to be measured between SHWFS centroids and DM actuator commands. The inverse of the interaction matrix can then be multiplied by on-sky SHWFS centroids to estimate the DM commands required for mitigating the observed wavefront perturbations. Atmospheric turbulence is driven by the wind meaning that wavefront measurements must be continuously translated into DM commands. However, due to systematic limitations, e.g. computer processing speeds, wavefront correction updates are not instantaneous.

Astronomical telescopes continue to play a significant role in the development of advanced AO systems. Ground-space FSOC AO systems can be related to these instruments however, they must consider the fact that they will often be operated in stronger turbulence conditions. A continental network will need multiple OGSs over a large area to avoid cloud cover limitations, helping ensure a constant line-of-sight to the spacecraft. The implication here is that a number of OGSs might be built in regions that are undesirable for astronomical telescopes. The atmospheric turbulence will be stronger at these locations [1]. Furthermore, daytime operation will be required to achieve 24-hour link availability - a time during which atmospheric turbulence can be significantly stronger [2]. In the presence of strong turbulence, phase differences in the propagating light can interfere and give rise to areas of the integrated wavefront having zero amplitude [3]. These amplitude fluctuations make it a challenge to measure wavefront phase and can therefore directly lead to a degradation in AO performance.

The structure of atmospheric turbulence can be visualized as a profile consisting of multiple discrete layers with every layer having an associated strength and velocity [4, 5]. The refractive index structure constant, $C_n^2(z)$, describes the strength of the turbulence profile, where z denotes the propagation distance from each layer to the observer. The Fried parameter describes the integrated coherence length at a specified wavelength, λ , and is given by [5, 6]

$$r_0 = \left[0.423 \left(\frac{2\pi}{\lambda} \right)^2 \sec(\beta) \int C_n^2(z) dz \right]^{-3/5}. \quad (1)$$

This study defines atmospheric parameters at $\lambda = 0.5 \mu\text{m}$. In Eq. 1 the zenith angle is given by β and therefore $\sec(\beta)$ is the air mass.

The required AO loop update rate is dependent on $C_n^2(z)$ and the wind-driven speed of each layer, $w_s(z)$. The coherence time, τ_0 , is commonly used to help determine an acceptable time delay, and is defined by the change in time that gives a residual mean square wavefront error equal to 1 radian. World-leading astronomical sites typically record τ_0 values around 3 ms (at $\lambda = 0.5 \mu\text{m}$) [7, 8]. A SHWFS can directly measure the coherence time however, this requires the SHWFS to sample the wavefront with a time step less than τ_0 . An alternative approach for calculating τ_0 is to directly measure the strength and speed of each turbulent layer. The turbulence and wind speed profile define the coherence time as [5]

$$\tau_0 = \left[2.914 \left(\frac{2\pi}{\lambda} \right)^2 \sec(\beta) \int C_n^2(z) w_s(z)^{5/3} dz \right]^{-3/5}. \quad (2)$$

Eq. 2 demonstrates that the coherence time can be calculated if an observer is able to

simultaneously measure turbulence profile strengths and their corresponding wind speeds. The integral is over the entire atmosphere meaning that every layer is included. It can be seen that both the turbulence and wind speed profile are a function of z . However, as long as each turbulence layer strength can be paired with its corresponding wind speed, the value of each propagation distance is irrelevant to the overall calculation of τ_0 , i.e. the integral in Eq. 2 is equivalent to the summation of each turbulence layer strength multiplied by its corresponding wind speed.

A complete ground-space FSO network must have bilateral communication (space-to-ground and ground-to-space). The downlink signal from the spacecraft can be observed at an OGS and AO used to perform wavefront correction. The wavefront measured from the downlink can then be used to pre-distort the uplink such that - after propagating through the atmosphere - a planar wavefront is received at the spacecraft. However, to compensate for the relative tangential velocity of the spacecraft and the finite speed of light, the uplink beam must be pointed ahead of the spacecraft. This ensures that the spacecraft and the optical beam intersect. The angular distance between the downlink and the uplink beam is referred to as the Point-Ahead Angle (PAA). The result of having a PAA is that the uplink travels through a different volume of turbulence than the downlink. How severely the pre-compensated uplink is degraded by the PAA depends on the distribution of turbulent layer strengths as a function of altitude.

The isoplanatic angle, θ_0 , can be used to parameterize the expected quality of uplink pre-compensation, and is defined as the angular offset from a line-of-sight that gives a residual Root Mean Square (RMS) wavefront error equal to 1 radian. The isoplanatic angle can be calculated from the turbulence profile structure using [5]

$$\theta_0 = \left[2.914 \left(\frac{2\pi}{\lambda} \right)^2 \sec^{8/3}(\beta) \int C_n^2(z) z^{5/3} dz \right]^{-3/5}. \quad (3)$$

Eq. 3 does not have any dependence on the speed of each layer. However, unlike Eq. 2, it is strictly dependent on knowing the propagation distance to each turbulent layer strength.

The key parameters for characterizing any observation site are r_0 (the integrated turbulence strength), τ_0 (the speed at which the turbulence is evolving) and θ_0 (the structure of the turbulence profile). Measuring these parameters in real-time is critical for AO performance verification and automated OGS site ranking, i.e. based on real-time atmospheric characterization updates, spacecraft can choose between OGSs and decide which channel would be best-suited for stable communication. Atmospheric profile information can also be used by predictive control algorithms to optimise AO performance [9]. It has recently been shown that AO controllers primed with turbulence and wind velocity profile information can significantly improve the observed Strehl ratio during satellite downlink [10]. Additionally, turbulence and wind velocity profile information assists the development, calibration and validation of forecasts [11–13]. Atmospheric profiling is therefore greatly important to both astronomy and ground-space FSO.

It is possible to measure the turbulence profile by fitting an analytical model to the cross-covariance of SHWFS phase gradient measurements [8, 14–18]. This widely used technique is known as Slope Detection and Ranging (SLODAR) [14]. An adaptation of the SLODAR technique has been used to show that the wind velocity profile can also be recovered from SHWFS measurements [8, 19]. These previous studies have focused on multi-source SHWFS measurements that allow for altitude information to be recovered from cross-beam triangulation. However, systems designed for ground-space FSO only observe a single-source: the downlink signal from the spacecraft. This requires continuous spacecraft tracking and so it is not possible to simultaneously use background stars for multi-source observations. Shown in Fig. 1 is an illustration of the optical paths associated with a single-source 14×14 SHWFS (dimensions in sub-apertures). The layer number is given by l .

A number of previous publications have already developed single-source profiling techniques for dedicated astronomical site characterization instruments [20–22]. The atmospheric scintillation

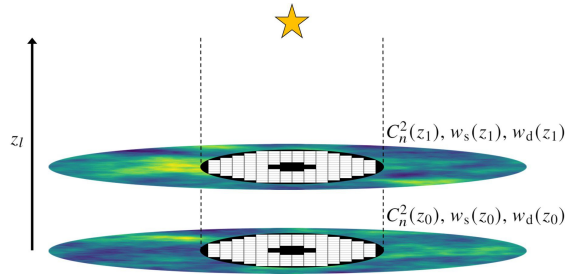


Fig. 1. Sub-aperture optical paths of a single-source 14×14 SHWFS. Two turbulent layers are shown at independent altitudes. The two black meta-pupils depict the SHWFS being conjugate to the pupil plane of the telescope.

is required as an input measurement to all of these techniques because this second order effect is correlated to both the strength and altitude of each turbulent layer. Understanding this phenomenon makes it possible to measure the turbulence profile structure by fitting theoretical response functions to on-sky data. The problem with these techniques is that their response functions are only valid in relatively weak turbulence regimes [22]. Therefore, the approach taken by current single-source profiling techniques is not considered applicable to the field of ground-space FSOC.

This study builds upon previous work [8, 18, 19] and introduces a novel technique for using a single-source SHWFS to track the strength and velocity of turbulent layers. The developed algorithm disentangles independent layers by fitting an analytical model to temporally offset SHWFS cross-covariance arrays. Simulated data is used to qualitatively test the technique and it is shown, over a range of turbulence conditions, that the algorithm is proficient at measuring both r_0 and τ_0 . The on-sky data required to run the fitting algorithm comes from SHWFS observations of a single-source celestial object, e.g. a star or the downlink signal from a Geosynchronous Equatorial Orbit (GEO) satellite. Objects that require relatively fast tracking, e.g. a Low Earth Orbit (LEO) satellite, are not currently considered because the technique assumes Taylor frozen-flow, and it is unclear whether this assumption is still valid if telescope slew is non-negligible.

The presented technique does not recover θ_0 because it does not measure the altitude of each layer. However, one of the significant outcomes of the work presented is that an algorithm has been developed that can use single-source SHWFS telemetry to detect the strength and velocity of independent layers. It is planned that future studies will build upon this work to show how these independent layer detections can be used to recover the turbulence profile structure. Such an achievement would dramatically aid both astronomy and ground-space FSOC.

2. Measuring the strength and velocity of atmospheric turbulence

2.1. Integrated turbulence

In an AO system the SHWFS is conjugate to the pupil plane of the telescope and the incoming light across each of its sub-apertures is focused onto a detector. The photon distribution of the focused light within each sub-aperture can then be used to calculate its x and y centroid. When monitoring a point source on-sky, SHWFS centroid movement is related to the integrated strength of the atmospheric turbulence along its line-of-sight. It can be assumed that the only other influencing factor are tip-tilt telescope vibrations that are caused by, e.g. wind shake. This study will therefore only consider open-loop SHWFS centroids that have been tip-tilt subtracted [15].

Sub-aperture centroids can be stacked into an array as the detector iterates over a number of frames. The resultant array will span a time length equal to Ω/f , where Ω is the total number of

frames iterated over and f is the frame rate of the detector. The cross-covariance of this SHWFS centroid array is referred to as the auto-covariance matrix. The auto-covariance matrix can be broken down into three regions: $\text{cov}(x, x)$, $\text{cov}(y, y)$ and $\text{cov}(x, y)$. The response between orthogonal axes has a relatively low Signal-to-Noise Ratio (SNR) and is therefore discarded [18]. Calculating the mean auto-covariance as a function of sub-aperture separation, for both $\text{cov}(x, x)$ and $\text{cov}(y, y)$, results in what is known as the auto-covariance map.

An example 14×14 SHWFS auto-covariance map is shown in Fig. 2. Its spatial resolution is a function of the distance between the centre of adjacent sub-apertures, s_w . Sub-aperture separations are considered in both x , x_{sep} , and y , y_{sep} . The left and right of Fig. 2 shows the mean auto-covariance for $\text{cov}(x, x)$ and $\text{cov}(y, y)$, respectively. Soapy, a Monte Carlo AO simulation package [23], generated the centroids used to calculate Fig. 2. The simulated atmosphere had $r_0 = 0.10$ m. The system parameters used in the Soapy configuration file are shown in Table 1 and are a constant throughout this study. These system parameters are representative of a typical OGS used for FSOC links with GEO satellites.

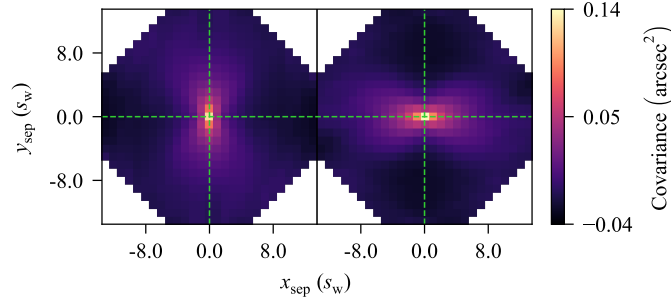


Fig. 2. A simulated 14×14 SHWFS auto-covariance map. Green dashed lines have been overlaid to indicate where $x_{\text{sep}} = y_{\text{sep}} = 0$.

Telescope diameter (m)	0.8
Frame rate (Hz)	500
Number of frames	10,000
Monochromatic wavelength (μm)	1.55

Table 1. System parameters used to simulate SHWFS data.

It is possible to analytically generate a tip-tilt subtracted auto-covariance map [14, 15]. This model can be used to perform a least-squares fit to, e.g. Fig. 2, by iteratively adjusting r_0 , resulting in a direct measurement of the integrated coherence length. This technique for measuring r_0 has been demonstrated by a number of previous studies [14–18].

Changes in turbulence strength scale linearly with the refractive index structure constant whereas r_0 follows a $-3/5$ power law (see Eq. 1). Therefore, to simplify comparisons between measured and expected values, this study defines the integrated optical turbulence profile strength, K_0 , where

$$K_0 = \sum_{l=0}^{\gamma} C_n^2(z_l). \quad (4)$$

The total number of layers is given by γ . Parameters measured when fitting to the auto-covariance

map are represented with the subscript c, e.g. $K_{0,c}$ is measured by performing a least-squares fit to Fig. 2. Only one layer needs to be fitted when measuring $K_{0,c}$.

It is recognized that the analytical model marginally overestimates spatial covariance [24]. This inaccuracy scales with the inverse of sub-aperture separation distance. Hence, when fitting to, e.g. Fig 2, the fitting algorithm inherently underestimates the integrated optical turbulence profile strength. Through simulation testing it was found that the outlined system can calibrate $K_{0,c}$ by increasing its measured value by 3%.

2.2. Disentanglement of discrete velocities

The discrete nature of turbulent layers means that they can be treated independently, i.e. when modeling auto-covariance, a three-layer map is calculated by the summation of three one-layer maps. Each layer of turbulence has a wind-driven velocity. To visualize the wind velocity of individual layers, the auto-covariance map can be calculated but with a temporal offset, δt , between SHWFS frames [19], where

$$\delta t = \omega / f. \quad (5)$$

In Eq. 5, ω is the number of frames that have been offset and f is the frame rate of the detector. Shown in Fig. 3 is the temporally offset auto-covariance map calculated from the simulated data used to calculate Fig. 2. There were three layers simulated and it is now possible to see each of these layers.

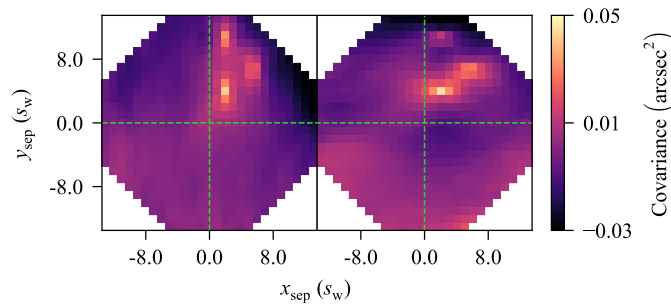


Fig. 3. Temporally offset auto-covariance map from the simulated data that was used to calculate Fig. 2. Three layers can now be identified due to their discrete velocities. Green dashed lines have been overlaid to indicate where $x_{\text{sep}} = y_{\text{sep}} = 0$.

2.3. Automated tracking of turbulent layers

The simulation from before was repeated but for one layer. The resulting temporally offset auto-covariance map is shown in Fig. 4.

The Levenberg–Marquardt algorithm is used throughout this study for all least-squares fitting. This algorithm can use the analytical model for auto-covariance generation to iteratively fit $x_{\text{sep}}(z_l)$, $y_{\text{sep}}(z_l)$ and $C_n^2(z_l)$ to the measured temporally offset auto-covariance map. The analytically generated auto-covariance map that was fitted to Fig. 4 is shown in Fig. 5.

Taylor frozen-flow [25] is assumed throughout this study. This assumption implies that the strength and velocity of each layer is conserved in the temporally offset auto-covariance map. Between Fig. 4 and Fig. 5 there is a change in x_{sep} and y_{sep} (Δx_{sep} and Δy_{sep} , respectively). At $\delta t = 0$, the peak cross-covariance strength for each layer is centred at $x_{\text{sep}} = y_{\text{sep}} = 0$ (see Fig. 2). Therefore, the wind direction of the fitted layer, $w_d(z_l)$, can be calculated from the magnitudes of $\Delta x_{\text{sep}}(z_l)$ and $\Delta y_{\text{sep}}(z_l)$. Its wind speed is equal to [19]

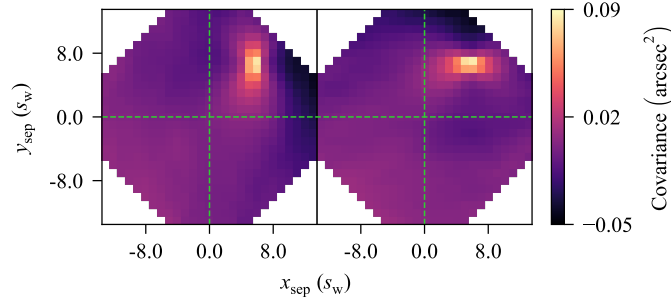


Fig. 4. Temporally offset auto-covariance map from a one-layer SHWFS simulation. Green dashed lines have been overlaid to indicate where $x_{\text{sep}} = y_{\text{sep}} = 0$.

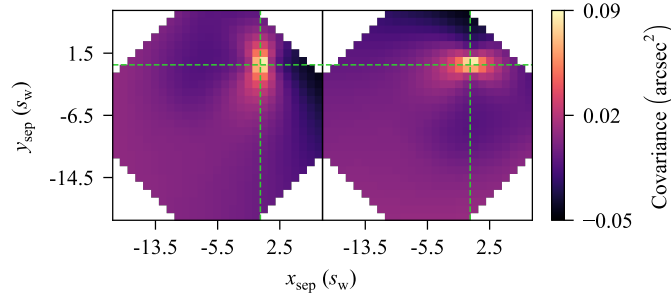


Fig. 5. The analytically generated auto-covariance map after iteratively fitting $x_{\text{sep}}(z_l)$, $y_{\text{sep}}(z_l)$ and $C_n^2(z_l)$ to the temporally offset auto-covariance map shown in Fig. 4. Green dashed lines have been overlaid to indicate where the analytical model has fitted $x_{\text{sep}}(z_l) = y_{\text{sep}}(z_l) = 0$.

$$w_s(z_l) = \frac{\sqrt{\Delta x_{\text{sep}}(z_l)^2 + \Delta y_{\text{sep}}(z_l)^2}}{\delta t}. \quad (6)$$

The example above is for a one-layer simulation however, the same logic can be applied to a multi-layer scenario. Each layer is statistically independent. Therefore, the analytical model can simultaneously fit $x_{\text{sep}}(z_l)$, $y_{\text{sep}}(z_l)$ and $C_n^2(z_l)$ - for multiple layers - to a multi-layer temporally offset auto-covariance map. The result from the fitting algorithm is an array of turbulence strengths with corresponding wind velocity measurements.

There is the possibility that two or more layers have similar wind velocities. This will give the appearance of a single layer in the temporally offset auto-covariance map. In this scenario the fitting algorithm might incorrectly detect a single layer at this location. The same is true vice-versa: the fitting algorithm might detect two or more layers where there is only one. It is important to note that, despite these occurrences, this behavior will not negatively influence the resulting τ_0 measurement.

Parameters measured when fitting to the temporally offset auto-covariance map are represented with the subscript m, e.g. $K_{0,m}$ is measured by performing a least-squares fit to Fig. 3.

2.3.1. Initial parameter estimates

The Levenberg–Marquardt algorithm is a least-squares fitting procedure that is used to find a local minimum. The algorithm must be given appropriate initial parameter estimates to ensure that all turbulent layers are accounted for at the local minimum it finds. This challenge is addressed by completing the fitting in three parts.

1. The analytical model is fitted to the auto-covariance map, e.g. Fig. 2, to recover the measured integrated optical turbulence profile strength, $K_{0,c}$.
2. Starting at zero sub-aperture separation, $x_{\text{sep}}(z_l)$ and $y_{\text{sep}}(z_l)$ are fitted to the temporally offset auto-covariance map, e.g. Fig. 3. The turbulence strength of each fitted layer remains a constant and is equal to $K_{0,c}/\gamma$, where γ denotes the total number of layers being fitted.
3. Using the results from 2 as initial parameter estimates: $x_{\text{sep}}(z_l)$, $y_{\text{sep}}(z_l)$ and $C_n^2(z_l)$ are all simultaneously fitted to the temporally offset auto-covariance map, e.g. Fig. 3.

2.3.2. Validating turbulent layer measurements

Least-squares fitting implies that there will always be a result for each fitted layer. A layer measurement can be immediately discarded if its displacement positions its cross-covariance peak outside of the auto-covariance map.

The user inputs how many layers the algorithm will fit. If there are more layers fitted than can be identified, e.g. if ten layers were fitted to Fig. 4, then there is an increased likelihood that the algorithm will suffer from overfitting. Therefore, it is important to constrain the fitted results. To do this the turbulent layer measurements are first ordered with respect to their wind speed. Preference is given to lower wind speeds because the SNR in the measured auto-covariance map decreases as a function of sub-aperture separation [18]. Consecutive layers are then considered valid until $K_{0,m} > K_{0,c}$. The remaining layers are discarded.

3. Results

The median 35-layer model from the European Southern Observatory (ESO) [26, 27] was used to parameterize the turbulence and wind speed profile for 256 Soapy simulations. This profile was selected to comply with previous publications [18, 19] and because it derives from on-sky atmospheric profiles. The data comes from around the site of the Very Large Telescope (VLT) in Paranal, Chile. This observatory is at 2664m. Models such as the Hufnagel-Valley profile [28] indicate that, compared to the 35-layer ESO model, the ground layers for a sea level observatory contain a higher fraction of the total integrated turbulence strength. However, it is important to note that this is a theoretical model and that at every site the turbulence profile is continuously changing [29].

At the start of each simulation an r_0 value between 0.05 and 0.15 m was randomly selected from a uniform distribution. This range of r_0 values was chosen because it covers typical conditions at world-leading astronomical observatories, as well as the stronger turbulence conditions that can be expected during ground-space FSOC [7, 30–32]. The strength of each layer was scaled accordingly such that, for each simulation, the total integrated strength of the profile was equivalent to the randomly selected r_0 value. The 35-layer wind direction profile was also randomly generated from a uniform distribution, i.e. each layer had a random wind direction between 0 and 360°.

Independent layers become easier to discern as the temporal offset between SHWFS measurements is increased. However, it must be ensured that the fastest layers will still be observed. The fastest wind speed in the 35-layer ESO profile is approximately 34 m/s. Hence, measurements were taken from fitting to a temporally offset covariance map with δt equal to 22 ms. Previous studies have indicated that - for tracking turbulent layers using the SLODAR technique - Taylor frozen-flow can be assumed up to approximately 50 ms [8, 19].

The three-step fitting procedure (see Section 2.3.1) was used to study the temporally offset auto-covariance maps from the simulated SHWFS centroids. For each simulation, measurements were made when fitting 1 to 35 layers. Results for the number of layers validated (see Section 2.3.2) are shown in Fig. 6.

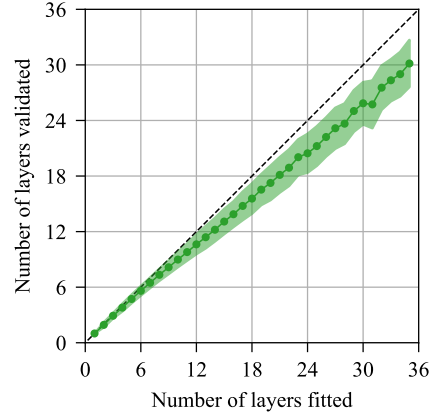


Fig. 6. The number of layers fitted against the number of layers validated. Circular markers show the mean. The shaded area plots the standard deviation. The black dashed line plots where the number of layers fitted equals the number of layers validated.

The simulated K_0 and τ_0 can be calculated from each of the 35-layer simulations. These simulated parameters are represented with the subscript n . The fractional difference between the measured and simulated K_0 is therefore $(K_{0,m} - K_{0,n})/K_{0,n}$. Using the fractional difference allows for the results from each simulation to be compared, despite each simulation having a different r_0 . The fractional difference results for K_0 and τ_0 are shown in Fig. 7.

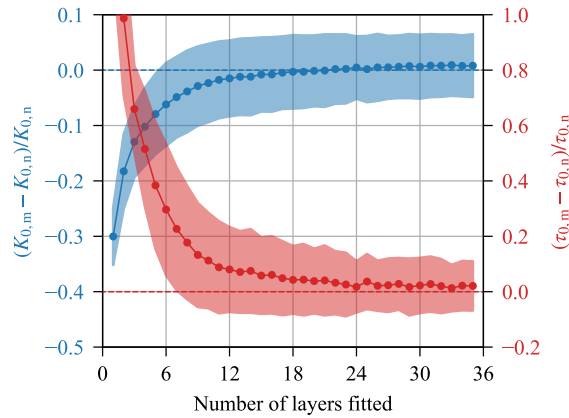


Fig. 7. The K_0 and τ_0 fractional difference between the measured and simulated values (in blue and red, respectively), shown as a function of the number of layers fitted. Circular markers show the mean. The shaded areas plot the standard deviation. Blue and red dashed lines plot zero fractional difference.

As mentioned in Section 2.3, the analytical model can use a single layer to represent multiple layers that overlap in the temporally offset auto-covariance map. Fig. 7 demonstrates that fitting

more than approximately 24 layers does not noticeably change the measurement accuracy of K_0 or τ_0 . On-sky measurements typically show gradual transitions between the wind direction of adjacent layers [33]. Therefore, because the wind direction profiles were randomly generated, it is concluded that the convergence observed in Fig. 7 indicates that this system would not have to fit more than 24 layers when studying on-sky data. The significance of requiring fewer layers is that the fitting algorithm is faster and therefore its output measurements are closer to real-time.

It can be seen in Fig. 7 that the algorithm begins to marginally overestimate $K_{0,m}$ when fitting more than 24 layers. This can be attributed to overfitting and the model not perfectly aligning to the measured values (as discussed in Section 2.3.2 and Section 2.1, respectively). However, it should be noted that this overestimation is equal to a fractional difference of approximately 0.01.

A scatter plot between the measured and simulated τ_0 ($\tau_{0,m}$ and $\tau_{0,n}$, respectively) is shown in Fig. 8. The results in this plot correspond to fitting 24 layers. The Pearson correlation coefficient is 0.95. It can be seen that the spread of data points is greater at larger values of r_0 . This is attributed to some of the layers having especially weak turbulence at these values of r_0 , making their strengths more difficult to accurately detect.

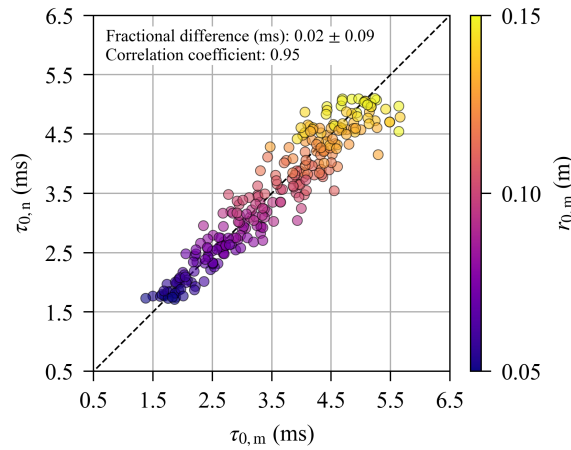


Fig. 8. Scatter plot of the measured and simulated coherence time ($\tau_{0,m}$ and $\tau_{0,n}$, respectively). The results correspond to the algorithm fitting 24 layers (see Fig. 7). The assigned colors show the measured integrated turbulence strength, $r_{0,m}$. The black dashed line plots where $\tau_{0,m}$ equals $\tau_{0,n}$.

4. Conclusion

The advancement of Earth-space communication is greatly dependent on FSOC. If this optical technology can be realized then future space missions will have a communication rate orders of magnitude greater than current RF channels. The outstanding challenge for ground-space FSOC is the fact that optical signals are critically perturbed by atmospheric turbulence. The profile of atmospheric turbulence can be modelled as discrete layers separated in altitude, with the turbulence at each altitude described in terms of both its strength and wind-driven velocity. Developments in advanced AO systems have proven that this technology can use real-time wavefront correction to mitigate atmospheric perturbations. These AO systems require atmospheric profile information to optimizing their control and operation.

Collectively, the strength and speed of each layer determines the rate at which the integrated wavefront error changes. This rate is parameterized by the coherence time, τ_0 . Typical AO telemetry atmospheric profiling techniques require multi-source targets for cross-beam

triangulation. However, there is only a single-source available during ground-space FSOC: the downlink signal from the spacecraft.

In this study a novel technique was introduced that is capable of using single-source SHWFS telemetry to measure turbulence profile strengths and their corresponding wind velocities. The technique is able to study the atmosphere by fitting an analytical model to temporally offset auto-covariance map measurements. The introduction of this technique is an important development for optimizing the operation of AO systems used for both astronomy and ground-space FSOC.

The fitting algorithm was tested by performing analysis on 256 simulations. These simulations emulated on-sky conditions by taking their atmospheric configuration from the median ESO 35-layer model. It was found that the measured results converged on the simulated values when the model fits approximately 24 layers. The simulated and measured coherence times were shown to have a correlation coefficient of 0.95. The developed algorithm must now study on-sky data to confirm that it remains robust while analyzing dynamic atmospheric profiles. Its performance during strong turbulence conditions must also be evaluated.

Further research will go towards demonstrating how this work can lead to a novel single-source profiling technique for recovering the altitude of each turbulence profile layer, thereby resulting in a direct measurement of the isoplanatic angle, θ_0 .

Acknowledgements

All of the plots were rendered in Matplotlib [34]. The data analysis software was written in Python using the NumPy and SciPy libraries [35, 36].

We thank the Federal Ministry for Economic Affairs and Energy (BMWi) for their support and for providing aid to industrial-related research in the course of the COVID-19 pandemic.

Disclosures

The authors declare no conflicts of interest.

Data availability

Data underlying the results presented in this paper are not publicly available at this time but may be obtained from the authors upon reasonable request.

References

1. J. Osborn, "Global turbulence forecasts using a general circulation model," in *Imaging and Applied Optics 2019 (COSI, IS, MATH, pcAOP)*, (Optical Society of America, 2019), p. PM3C.4.
2. J. M. de la Rosa, L. Montoya, M. Collados, I. Montilla, and N. V. Reyes, "Daytime turbulence profiling for EST and its impact in the solar MCAO system design," in *Adaptive Optics Systems V*, vol. 9909 E. Marchetti, L. M. Close, and J.-P. Véran, eds., International Society for Optics and Photonics (SPIE, 2016), pp. 2035 – 2048.
3. D. W. Oesch, D. J. Sanchez, and C. L. Matson, "The aggregate behavior of branch points - measuring the number and velocity of atmospheric turbulence layers," *Opt. Express* **18**, 22377–22392 (2010).
4. A. Kolmogorov, "The Local Structure of Turbulence in Incompressible Viscous Fluid for Very Large Reynolds' Numbers," *Akademiia Nauk SSSR Doklady* **30**, 301–305 (1941).
5. F. Roddier, *Adaptive Optics in Astronomy* (Cambridge University Press, 1999).
6. D. L. Fried, "Statistics of a Geometric Representation of Wavefront Distortion," *J. Opt. Soc. Am.* (1917-1983) **55**, 1427–1431 (1965).
7. J. Osborn, R. W. Wilson, M. Sarazin, T. Butterley, A. Chacón, F. Derie, O. J. D. Farley, X. Haubois, D. Laidlaw, M. LeLouarn, E. Masciadri, J. Milli, J. Navarrete, and M. J. Townson, "Optical turbulence profiling with Stereo-SCIDAR for VLT and ELT," *Mon. Notices Royal Astron. Soc.* **478**, 825–834 (2018).
8. D. J. Laidlaw, "Turbulence and wind velocity profiles from adaptive optics telemetry: a general and scalable solution for extremely large telescopes," Ph.D. thesis, Durham University (2020).
9. K. Jackson, C. Correia, O. Lardière, D. Andersen, and C. Bradley, "Linear prediction of atmospheric wave-fronts for tomographic adaptive optics systems: modelling and robustness assessment," *Opt. Lett.* **40**, 143–146 (2015).
10. L. Prengère, C. Kulcsár, and H.-F. Raynaud, "Zonal-based high-performance control in adaptive optics systems with application to astronomy and satellite tracking," *J. Opt. Soc. Am. A* **37**, 1083–1099 (2020).

11. E. Masciadri, F. Lascaux, and L. Fini, "MOSE: operational forecast of the optical turbulence and atmospheric parameters at European Southern Observatory ground-based sites - I. Overview and vertical stratification of atmospheric parameters at 0-20 km," *Mon. Notices Royal Astron. Soc.* **436**, 1968–1985 (2013).
12. G. Sivo, A. Turchi, E. Masciadri, A. Guesalaga, and B. Neichel, "Towards an automatic wind speed and direction profiler for Wide Field adaptive optics systems," *Mon. Notices Royal Astron. Soc.* **476**, 999–1009 (2018).
13. J. Osborn and M. Sarazin, "Atmospheric turbulence forecasting with a general circulation model for Cerro Paranal," *Mon. Notices Royal Astron. Soc.* **480**, 1278–1299 (2018).
14. R. W. Wilson, "SLODAR: measuring optical turbulence altitude with a Shack–Hartmann wavefront sensor," *Mon. Notices Royal Astron. Soc.* **337**, 103–108 (2002).
15. T. Butterley, R. W. Wilson, and M. Sarazin, "Determination of the profile of atmospheric optical turbulence strength from SLODAR data," *Mon. Notices Royal Astron. Soc.* **369**, 835–845 (2006).
16. A. Guesalaga, B. Neichel, A. Cortés, C. Béchet, and D. Guzmán, "Using the C_n^2 and wind profiler method with wide-field laser-guide-stars adaptive optics to quantify the frozen-flow decay," *Mon. Notices Royal Astron. Soc.* (2014).
17. O. A. Martin, C. M. Correia, E. Gendron, G. Rousset, F. Vidal, T. J. Morris, A. G. Basden, R. M. Myers, Y. H. Ono, B. Neichel, and T. Fusco, "William herschel telescope site characterization using the moao pathfinder canary on-sky data," (2016), pp. 9909 – 9909 – 15.
18. D. J. Laidlaw, J. Osborn, T. J. Morris, A. G. Basden, O. Beltramo-Martin, T. Butterley, E. Gendron, A. P. Reeves, G. Rousset, M. J. Townson, and R. W. Wilson, "Optimizing the accuracy and efficiency of optical turbulence profiling using adaptive optics telemetry for extremely large telescopes," *Mon. Notices Royal Astron. Soc.* **483**, 4341–4353 (2018).
19. D. J. Laidlaw, J. Osborn, T. J. Morris, A. G. Basden, E. Gendron, G. Rousset, M. J. Townson, and R. W. Wilson, "Automated wind velocity profiling from adaptive optics telemetry," *Mon. Notices Royal Astron. Soc.* **491**, 1287–1294 (2019).
20. A. Habib, J. Vernin, Z. Benkhaldoun, and H. Lanteri, "Single star scidar: atmospheric parameters profiling using the simulated annealing algorithm," *Mon. Notices Royal Astron. Soc.* **368**, 1456–1462 (2006).
21. N. Védrenne, V. Michau, C. Robert, and J. Conan, "Cn2 profile measurement from shack-hartmann data," *Opt. Lett.* **32**, 2659–2661 (2007).
22. A. Tokovinin and V. Kornilov, "Accurate seeing measurements with MASS and DIMM," *Mon. Notices Royal Astron. Soc.* **381**, 1179–1189 (2007).
23. A. Reeves, "Soapy: an adaptive optics simulation written purely in Python for rapid concept development," in *Adaptive Optics Systems V*, vol. 9909 E. Marchetti, L. M. Close, and J.-P. Véran, eds., International Society for Optics and Photonics (SPIE, 2016), pp. 2173 – 2183.
24. O. Martin, Éric Gendron, G. Rousset, and F. Vidal, "Temporal convergence of phase spatial covariance matrix measurements in tomographic adaptive optics," in *Adaptive Optics Systems III*, vol. 8447 International Society for Optics and Photonics (SPIE, 2012), pp. 855–868.
25. G. I. Taylor, "The Spectrum of Turbulence," *Proc. Royal Soc. Lond. Ser. A* **164**, 476–490 (1938).
26. M. Sarazin, M. Le Louarn, J. Ascenso, G. Lombardi, and J. Navarrete, "Defining reference turbulence profiles for E-ELT AO performance simulations," in *Proceedings of the Third AO4ELT Conference*, S. Esposito and L. Fini, eds. (2013), p. 89.
27. O. J. D. Farley, J. Osborn, T. Morris, T. Fusco, B. Neichel, C. Correia, and R. W. Wilson, "Limitations imposed by optical turbulence profile structure and evolution on tomographic reconstruction for the ELT," *Mon. Notices Royal Astron. Soc.* **494**, 2773–2784 (2020).
28. L. C. Andrews, R. L. Phillips, D. Wayne, T. Leclerc, P. Sauer, R. Crabbs, and J. Kiriazes, "Near-ground vertical profile of refractive-index fluctuations," in *Atmospheric Propagation VI*, vol. 7324 L. M. W. Thomas and G. C. Gilbreath, eds., International Society for Optics and Photonics (SPIE, 2009), pp. 11 – 22.
29. O. J. D. Farley, J. Osborn, T. Morris, M. Sarazin, T. Butterley, M. J. Townson, P. Jia, and R. W. Wilson, "Representative optical turbulence profiles for ESO Paranal by hierarchical clustering," *Mon. Notices Royal Astron. Soc.* **481**, 4030–4037 (2018).
30. M. Knappek, J. Horwath, N. Perlot, and B. Wilkerson, "The DLR ground station in the optical payload experiment (STROPEX): results of the atmospheric measurement instruments," in *Free-Space Laser Communications VI*, vol. 6304 A. K. Majumdar and C. C. Davis, eds., International Society for Optics and Photonics (SPIE, 2006), pp. 494 – 504.
31. D. Giggenbach, "Deriving an estimate for the fried parameter in mobile optical transmission scenarios," *Appl. Opt.* **50**, 222–226 (2011).
32. Kellerer, A., Gorceix, N., Marino, J., Cao, W., and Goode, P. R., "Profiles of the daytime atmospheric turbulence above big bear solar observatory," *A @ AND@A* **542**, A2 (2012).
33. J. Osborn, T. Butterley, M. J. Townson, A. P. Reeves, T. J. Morris, and R. W. Wilson, "Turbulence velocity profiling for high sensitivity and vertical-resolution atmospheric characterization with Stereo-SCIDAR," *Mon. Notices Royal Astron. Soc.* **464**, 3998–4007 (2016).
34. J. D. Hunter, "Matplotlib: A 2d graphics environment," *Comput. Sci. & Eng.* **9**, 90–95 (2007).
35. C. R. Harris, K. J. Millman, S. J. van der Walt, R. Gommers, P. Virtanen, D. Cournapeau, E. Wieser, J. Taylor, S. Berg, N. J. Smith, R. Kern, M. Picus, S. Hoyer, M. H. van Kerkwijk, M. Brett, A. Haldane, J. F. del R'io, M. Wiebe,

- P. Peterson, P. G'érard-Marchant, K. Sheppard, T. Reddy, W. Weckesser, H. Abbasi, C. Gohlke, and T. E. Oliphant, "Array programming with NumPy," *Nature* **585**, 357–362 (2020).
36. P. Virtanen, R. Gommers, T. E. Oliphant, M. Haberland, T. Reddy, D. Cournapeau, E. Burovski, P. Peterson, W. Weckesser, J. Bright, S. J. van der Walt, M. Brett, J. Wilson, K. J. Millman, N. Mayorov, A. R. J. Nelson, E. Jones, R. Kern, E. Larson, C. J. Carey, Í. Polat, Y. Feng, E. W. Moore, J. VanderPlas, D. Laxalde, J. Perktold, R. Cimrman, I. Henriksen, E. A. Quintero, C. R. Harris, A. M. Archibald, A. H. Ribeiro, F. Pedregosa, P. van Mulbregt, and SciPy 1.0 Contributors, "SciPy 1.0: Fundamental Algorithms for Scientific Computing in Python," *Nat. Methods* **17**, 261–272 (2020).

OPTICA
PUBLISHING GROUP
Formerly OSA